

# NMR Phase Error Correction with New Modelling Approaches

DOI: 10.47852/bonviewJDSIS42024036



Aixiang Jiang<sup>1,2,3,\*</sup>, Andrée E. Gravel<sup>4</sup>, Ethan Tse<sup>3</sup>, Sanjoy Kumar Das<sup>4</sup>, James Hanley<sup>1,5</sup>, and Robert Nadon<sup>6,\*</sup>

<sup>1</sup>Department of Epidemiology, Biostatistics, and Occupational Health, McGill University, Canada

<sup>2</sup>Department of Pathology and Laboratory Medicine, University of British Columbia, Canada

<sup>3</sup>British Columbia Cancer Centre for Lymphoid Cancer, Canada

<sup>4</sup>Proteomics and Molecular Analysis Platform, Research Institute McGill University Health Centre, Canada

<sup>5</sup>Department of Mathematics and Statistics, McGill University, Canada

<sup>6</sup>Department of Human Genetics, McGill University, Canada

\*Corresponding authors: Aixiang Jiang, Department of Epidemiology, Biostatistics, and Occupational Health, McGill University, Department of Pathology and Laboratory Medicine, University of British Columbia and British Columbia Centre for Lymphoid Cancer, Canada. Email: [aijiang@bccrc.ca](mailto:aijiang@bccrc.ca) and Robert Nadon, Department of Human Genetics, McGill University, Canada. Email: [robert.nadon@McGill.Ca](mailto:robert.nadon@McGill.Ca).

**Abstract:** Nuclear Magnetic Resonance (NMR) spectroscopy is a highly sensitive analytical technique essential for precise molecular identification and quantification. However, accurate results depend on effective pre-processing to correct for various types of errors. Phase error correction, in particular, is crucial for ensuring the reliability of NMR data. Current methods often rely on a single linear model, which may not adequately address all types of phase errors. As a result, this limitation frequently requires manual intervention, making the process both time-consuming and prone to errors. To address these limitations, we propose three modelling approaches for NMR phase error correction: nonlinear shrinkage, multiple models, and a new optimization function called delta absolute net minimization (DANM). Our comparison of seven methods revealed that nonlinear shrinkage outperformed others in both simulated spectra and a diabetes study, followed by multiple models with DANM. Additionally, our spike-in experiments demonstrated that DANM performed quite well in both single and multiple models. Our nonlinear shrinkage approach is a simple yet effective solution. We provide an open-source R package, NMRphasing, available on CRAN (<https://cran.r-project.org/web/packages/NMRphasing/>) and on GitHub (<https://github.com/aijiangsfu/NMRphasing>).

Keywords: NMR, phase error correction, nonlinear shrinkage, optimization, delta absolute net minimization (DANM)

## 1. Introduction

Nuclear magnetic resonance (NMR) applies the electromagnetic properties of atomic nuclei to diverse fields, including chemistry, physics, biology, material science, and engineering [1-22]. When samples are exposed to a strong magnetic field and a radio frequency pulse, certain atomic nuclei are temporarily excited to a higher energy state. As these nuclei relax back to their original, lower energy state, they emit radio frequency signals, which are detected and used to produce raw time-domain data [23]. These data are then Fourier transformed to produce frequency-domain spectral data, where the peaks are used to identify and quantify the molecules within the sample. However, if left uncorrected, the shapes and locations of the spectral peaks can be inaccurate due to unavoidable errors during signal

acquisition.

To address these challenges, this paper introduces NMR signals and phase error issues, reviews current correction methods, proposes new correction approaches, and evaluates the proposed correction approaches through simulations, a case study, and two spike-in experiments.

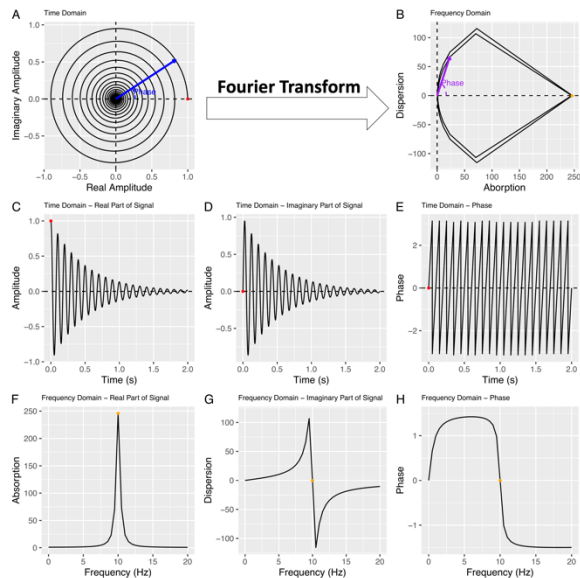
### 1.1. NMR signals and phase error challenges

NMR raw data are recorded with complex numbers to represent nuclei energy changes in two orthogonal directions, as shown in Figure 1A. Phase, which refers to the timing or position within a time-domain signal, is an important source of error in NMR. Phase is defined as the angle between a data point's vector and the x-axis in the complex plot, as illustrated in blue in Figure 1A.

Mathematically, it is expressed as the inverse tangent of the ratio of the imaginary part to the real part:  

$$\text{Phase} = \tan^{-1} \frac{\text{Imaginary}}{\text{Real}}$$

**Figure 1**  
**Illustration of NMR data with a simulated signal**



(A) Time domain complex plot. X-axis: Real amplitude, Y-axis: Imaginary amplitude. (B) Frequency domain complex plot. X-axis: Absorption - real intensity, Y-axis: Dispersion - imaginary intensity. In both (A) and (B), arrows show vectors of example data points, and the angles between the vectors and the X-axes are the corresponding phase values. (C) Time domain - Real part of the signal. (D) Time domain - Imaginary part of the signal. (E) Time domain - Phase. The X-axis in (C-E) is time in seconds. (F) Frequency domain - Absorption. (G) Frequency domain - Dispersion. (H) Frequency domain - Phase. The X-axis in (F-H) is frequency (Hz), where 1 Hz is cycles per second. Red dots in (A, C-E) indicate the first data point in the time domain, while orange dots in (B, F-H) show the peak maximum point.

With a Fourier transform, the time-domain data in Figure 1A are converted into frequency-domain data (Figure 1B). Frequency-domain data are also represented by complex numbers, where the real part corresponds to *absorption* and the imaginary part corresponds to *dispersion*. The definition of phase remains the same in the frequency domain, still representing the angle between a data point's vector and the x-axis, as shown in purple in Figure 1B.

Furthermore, each component of the time-domain data (Figure 1A) can be plotted separately, resulting in the real part, imaginary part, and phase plots shown in Figures 1C-E. The red starting point in Figure 1A corresponds to the maximum amplitude in the real part (Figure 1C), with an imaginary amplitude of zero (Figure 1D) and a phase value of zero (Figure 1E), as:  $\tan^{-1}\left(\frac{0}{\max(\text{amplitude})}\right) = \tan^{-1}(0) = 0$ . Similarly, for the frequency-domain data (Figure 1B), we can plot the absorption, dispersion, and phase separately, as

shown in Figures 1F-H. The orange point with the maximum absorption value in Figure 1B corresponds to the maximum absorption shown in Figure 1F, with zero dispersion in Figure 1G and a phase value of zero in Figure 1H.

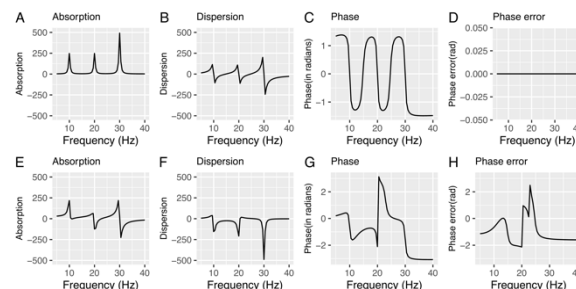
Phase errors represent discrepancies between the measured and true phase values [24]. These errors primarily arise from factors such as field distortions and eddy currents [25], as well as baseline correction processes that may inadvertently alter phase values. Noise and distortions during signal acquisition further contribute to phase errors, impacting the accuracy of phase measurements [24].

Phase cycling has been proposed as an efficient method for addressing phase errors [25, 26]. However, repeating experiments with multiple phase pulses is often too costly, and such data are rarely available.

There are three types of phase errors. Zero-order phase errors introduce a constant phase shift across the spectrum, while first-order phase errors cause a linear phase shift that varies with frequency. Nonlinear phase errors, on the other hand, produce phase shifts that vary in a more complex, nonlinear manner as the frequency changes [27].

In ideal conditions, when there are no phase errors, NMR signal analysis can focus on the real part in the frequency domain because real part peaks are sharp, concentrated, and easier to quantify, as shown in Figure 1F. The position of the absorption peak is used for molecule identification, while the area under the peak's curve is used for quantification. Even when multiple signals are present, as shown in Figures 2A-D, the absorption spectrum (Figure 2A) is still relied upon for identification and quantification.

**Figure 2**  
**Illustration of NMR phase errors in the frequency domain**



Panels A-D show simulated frequency domain absorption, dispersion, phase, and phase error plots without phase errors. Panels E-H show simulated frequency domain absorption, dispersion, phase, and phase error plots with phase errors.

However, real-world NMR data often contain phase errors, which distort the real parts and lead to a nonlinear combination of pure absorption and pure dispersion. This results in distorted absorption peaks, as shown in Figure 2E. The observed dispersion is also affected, as seen in Figure 2F. The phase pattern (Figure 2G) deviates significantly from the ideal phase pattern (Figure 2C). These phase errors

(Figure 2H) affect both the accuracy of peak location and the area under the curves (Figure 2E), making molecule identification and quantification unreliable.

Correcting phase errors before analysis is essential to ensure accurate results [24, 28]. Although various correction approaches have been proposed, there is no consensus on a universal protocol, highlighting the challenges posed by phase errors [29]. The lack of standardized correction methods necessitates further research to develop effective, tailored strategies that can adapt to the specific characteristics of different datasets. In the following sections, we will review existing phase error correction methods and propose our own approaches.

## 1.2. Current phase Error correction methods

Most existing methods for NMR phase error correction rely on a linear model to address phase errors [26, 30-41]. These methods account for zero-order and first-order phase errors by assuming a linear relationship between phase error and frequency. In NMR, *frequency* represents both the number of cycles per second in the time domain and the position of a signal's peak in the frequency domain.

For example, in Figure 1C, a signal with a frequency of 10 cycles per second corresponds to a peak at 10 Hz (Hertz, indicating cycles per second) in Figure 1F. Frequency-domain data are indexed by frequency, with a linear relationship between the data index (from 1 to N, where N is the total number of data points) and frequency. To simplify analysis, a scaled data index is often used to represent frequency in phase error correction models, expressed as [31]:

$$P_c \sim b_0 + b_1 \times f \quad (1)$$

where  $f$  is the scaled data index related to frequency, and  $b_0$  and  $b_1$  represent the intercept and slope, respectively.

However, this linear assumption fails to address nonlinear phase errors, as illustrated in Figure 2H. While earlier computational limitations hindered the development of more complex models, recent efforts have proposed higher-order polynomial models to incorporate local phase variations [27, 39, 42-47]. Unfortunately, these models often fall short in fully correcting phase errors, particularly in the presence of baseline bias and noise. Furthermore, the inclusion of higher-order terms in linear models tends to be unreliable [27].

Since the dependent variable, the phase correction value ( $P_c$ ), is unobservable, regression techniques are not applicable, making optimization necessary. This optimization process can be slow. To accelerate it, a recent approach involves optimizing a linear phase correction model using only two peaks [36]. While this method increases speed, it is less efficient, leading us to advise against its use.

Many algorithms employ various optimization functions to conduct the optimization process efficiently while

maintaining good quality [23, 30-33, 35, 48-50]. However, no single optimization function can effectively optimize the parameters of linear models to correct all phase errors.

Of the 20 optimization functions we reviewed [51], 15 primarily work with a linear model, with a few incorporating higher-order terms. These functions can be grouped as follows:

- (1) Integral of the imaginary component [52]
- (2) Integral of the real or absolute real part [32, 43, 53, 54]
- (3) Entropy-based [31, 52]
- (4) Absolute errors or squared errors [30, 34, 35, 38, 39, 54, 55]
- (5) Bayesian approach [49]
- (6) Pearson correlation between absorption and magnitude spectra [40]

Approaches based on absolute or squared errors rely on ground truth, which is difficult to obtain for real-world data. Bayesian approaches require extensive model assumptions, and Pearson correlation is inadequate because the relationship between absorption and magnitude spectra is nonlinear.

Given the limitations of these three groups of optimization functions, we have decided to focus our analysis on the remaining three groups—namely, the integral of the imaginary component, the integral of the real or absolute real part, and entropy-based methods—as a basis for comparing them with our new approaches.

Studies suggest that entropy-based methods [31] often outperform other approaches [56, 57]. However, even these methods fail to comprehensively correct all phase errors.

In summary, current phase error correction methods face three primary challenges:

- They often rely on only one part of complex data, resulting in information loss.
- A single linear model, even with higher-order terms, cannot fully correct all phase errors.
- No individual optimization function can adequately optimize linear model parameters to correct all phase errors.

As a result, manual adjustments are frequently necessary following automated phase correction or as a standalone process [50, 58-62]. However, manual phase error correction is time-consuming and relies on the personal experiences of experts, making it difficult to reproduce and potentially unreliable.

Recently, neural networks have been applied to phase error correction [45, 47, 63-65]. While this approach shows promise in addressing nonlinear phase errors, phase errors can vary significantly based on NMR machines, sample types, and measurement conditions [27]. Without a diverse and extensive training dataset, neural networks struggle to generalize effectively.

Furthermore, for neural networks to be effective, they require a well-defined loss function. Current loss functions

are typically based on absolute or squared errors, which rely on ground truth spectral data and their associated phases, often unavailable. Simulations or manually phased spectra are frequently used as substitutes for ground truth [45, 66], but they serve only as approximations.

These issues can result in noticeable phase errors that may persist even after neural network-based phasing [63, 65].

In this study, we concentrate on developing phase correction models and a new optimization function. Both approaches can be employed for traditional statistics-based phase error correction and integrated with neural networks to further improve phase error correction.

## 2. Approaches

We propose two novel modeling approaches to overcome specific limitations in current phase error correction methods: (1) a nonlinear intensity shrinkage method that utilizes both absorption and dispersion spectra, and (2) multiple models to handle different signals separately. We also present a new optimization function that simultaneously considers both positive and negative values as well as peak shapes.

### 2.1. Nonlinear intensity shrinkage

While traditional methods struggle to correct phase errors through optimization, our shrinkage method leverages theoretically phase-error-free spectra to estimate the real part of signals without requiring a complex optimization process for phase error correction.

Absorption (A) and dispersion (D) spectra represent the real and imaginary parts of NMR frequency domain data, respectively. Two important quantities in our model, the magnitude (M) and power (P) spectra, are derived from these components. The magnitude (M) is the absolute value of a complex number:  $\sqrt{A^2 + D^2}$ , and the power (P) is the squared value of M, reflecting the sum of the squares of the real (A) and imaginary (D) parts. Both M and P are theoretically free of phase errors and relate to A and D via the Pythagorean theorem

([https://en.wikipedia.org/wiki/Pythagorean\\_theorem](https://en.wikipedia.org/wiki/Pythagorean_theorem)):

$$P = M^2 = A^2 + D^2 \quad (2)$$

At any index k, and a phase value at k:  $\theta_k$ , we have:

$$\begin{aligned} A_k &= M_k \cos \theta_k \\ D_k &= M_k \sin \theta_k \end{aligned}$$

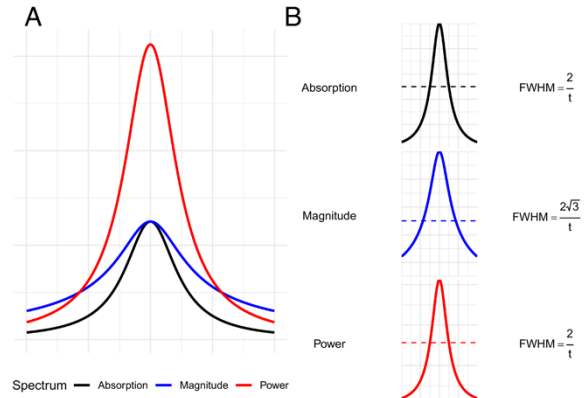
Using equation (2), we can express  $P_k$  as:

$$\begin{aligned} P_k &= A_k^2 + D_k^2 \\ &= (M_k \cos \theta_k)^2 + (M_k \sin \theta_k)^2 \\ &= M_k^2 ((\cos \theta_k)^2 + (\sin \theta_k)^2) \\ &= M_k^2 \end{aligned}$$

This proves that P and M are independent of the phase  $\theta$ , and thus, they are not affected by phase errors in theory.

Figure 3A demonstrates the comparable shapes and widths of the power peak and its corresponding absorption peak, while the magnitude peak matches the height of its corresponding absorption peak. Additionally, as shown in Figure 3B, the calculation formula for the full width at half maximum (FWHM), which is used to measure two times the shape parameter (scale) for a Cauchy-Lorentzian function often employed to describe a phase error-free signal, is identical for both power and absorption peaks.

**Figure 3**  
Comparison of different peak modes



(A) Absorption, magnitude, and power modes of a simulated ideal peak. (B) Full width at half maximum (FWHM) for ideal absorption, magnitude, and power modes. The plot is re-generated based on the concept from previous research [67].  $t$  represents the relaxation time.

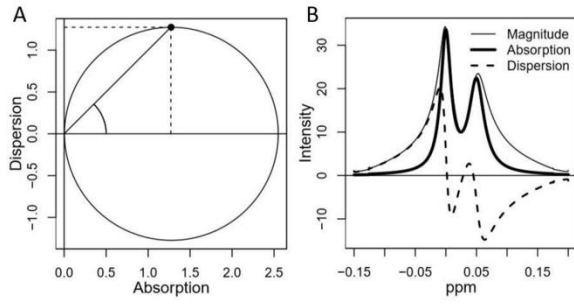
Based on these characteristics, our nonlinear intensity shrinkage method allows one to derive absorption spectra from phase-free magnitude and power spectra, enabling phase error correction without optimization. Our shrinkage method estimates absorption peaks within sub-ranges defined by major peaks, utilizing continuous wavelet transform-based pattern matching (Supplement 1). A shrinkage formula is employed to estimate absorption intensity to ( $A'_{k_l}$ ) for each data point within a sub-range:

$$A'_{k_l} = P_{k_l} \times \frac{\max(\overline{M}_l)}{\max(\overline{P}_l)} \quad (3)$$

In this formula,  $P_{k_l}$  represents the power intensity for the  $k$ th data point within the  $l$ th sub-range of a spectrum,  $\max(\overline{M}_l)$  represents the maximum magnitude intensity for the  $l$ th sub-range, and  $\max(\overline{P}_l)$  represents the maximum power intensity for the  $l$ th sub-range. The shrinkage process is applied separately to each sub-range, resulting in a nonlinear shrinkage for the entire spectrum. Detailed implementation for the shrinkage method can be found in Supplement 1.

**Figure 4**  
Relationships among simulated absorption, dispersion,

## and magnitude



(A) DISPA (dispersion vs absorption) circle: The x-axis shows absorption and the y-axis shows dispersion. The line from the black point to the origin (0,0) indicates a 45-degree phase, with its length representing magnitude.

(B) Two Overlapping Peaks: The left peak's magnitude equals its absorption height, while the right peak's magnitude is slightly taller, with slightly different ppm locations.

## Mathematical proof

The mathematical basis for the nonlinear shrinkage method can be illustrated using Figure 4A. The DISPA (dispersion vs. absorption) circle for a single peak without any error is depicted, with the center of the circle on the x-axis and its radius being  $\max M/2$ . The circle function is:

$$(x - \max M/2)^2 + y^2 = (\max M/2)^2$$

This can be rearranged to:

$$\begin{aligned} \rightarrow x^2 + (\max M/2)^2 - x \cdot \max M + y^2 &= (\max M/2)^2 \\ \rightarrow x^2 - x \cdot \max M + y^2 &= 0 \\ \rightarrow y^2 &= -x^2 + x \cdot \max M \\ \rightarrow y^2 &= x(\max M - x) \end{aligned} \quad (4)$$

In the above,  $x$  represents absorption,  $y$  represents dispersion, and  $\max M$  represents the peak height.

Furthermore, we always have the following based on equation (2):

$$A_k^2 + D_k^2 = M_k^2$$

Using annotation:  $A_k \rightarrow x$ ,  $D_k \rightarrow y$ ,  $M_k \rightarrow M$ , we have:

$$\begin{aligned} x^2 + y^2 &= M^2 \\ \rightarrow y^2 &= M^2 - x^2 \end{aligned} \quad (5)$$

By combining equations (4) and (5), we obtain:

$$\begin{aligned} x(\max M - x) &= M^2 - x^2 \\ \rightarrow x \cdot \max M - x^2 &= M^2 - x^2 \\ \rightarrow x \cdot \max M &= M^2 \end{aligned}$$

Thus:

$$\rightarrow x = M^2 / \max M \quad (6)$$

Here,  $\max M$  is the maximum magnitude (i.e., the peak height for the non-overlapping peak, which is a constant for a given peak range). Both  $x$  and  $M$  are variables representing values in the absorption and magnitude spectra, respectively.

For each point  $k_i$  in the  $l$ th sub-range, if we replace  $x$  with  $A'_{k_i}$ , write  $\max M$  more explicitly as  $\max(\vec{M}_l)$ , and replace  $M^2$  with the power value  $P_{k_i}$ ; equation (6) can be rewritten as follows:

$$A'_{k_i} = P_{k_i} / \max(\vec{M}_l)$$

$$= P_{k_i} \times \frac{\max(\vec{M}_l)}{\max(\vec{M}_l)} \times \frac{1}{\max(\vec{M}_l)}$$

$$= P_{k_i} \times \frac{\max(\vec{M}_l)}{(\max(\vec{M}_l))^2}$$

Since  $(\max(\vec{M}_l))^2 = \max(\vec{P}_l)$ , we obtain:

$$A'_{k_i} = P_{k_i} \times \frac{\max(\vec{M}_l)}{\max(\vec{P}_l)}$$

This confirms our proof of formula (3).

The ratio on the right side of formula (3) represents a shrinkage formula because for any number  $C$ , if  $C > 1$ ,  $C/(C^2) = 1/C < 1$ . The shrinkage factor  $\frac{\max(\vec{M}_l)}{\max(\vec{P}_l)}$  acts as a constant coefficient applicable for a given sub-range. The local maximum in a magnitude sub-range is positive and almost always bigger than 1 (In theory, it could be  $\leq 1$ , but we have not observed this situation in real nuclear magnetic resonance (NMR) data). Therefore, we consider  $\frac{\max(\vec{M}_l)}{\max(\vec{P}_l)}$  to represent linear shrinkage transformation.

Our approach operates on multiple sub-ranges by applying linear shrinkage within each sub-range; however, it represents nonlinear shrinkage for the entire spectrum, as each sub-range has its own shrinkage factor, which does not follow linear correlation.

When multiple peaks exist within a given range, the tallest peak retains the same height between its absorption peak and its magnitude peak. For nearby partially overlapping peaks, their absorption peaks are typically slightly shorter than their corresponding magnitude peaks, and the local maxima of these absorption peaks shift slightly towards the largest maximum peak among the overlapping peaks. This position change is minimal, typically just one index difference for the right-side peak illustrated in Figure 4B.

The minor height discrepancy between magnitude and absorption peaks for non-maximum peaks can be partially addressed by separating the spectra into sub-ranges based on major peaks. For example, the two peaks in Figure 4B are combined into one sub-range. Consequently, each sub-range undergoes shrinkage with the factor  $\frac{\max(\vec{M}_l)}{\max(\vec{P}_l)}$  applied within its range. This guarantees that the shrinkage factors for non-maximum peaks within the sub-range exceed those that would apply to each peak individually, resulting in slightly shorter estimated absorption peaks compared to their corresponding magnitude peaks. This aligns with our objective. Regarding the slight maximum location shift (e.g., one index difference for the small peak depicted in Figure 4B), this represents a minor concern for high-resolution NMR data, where two neighboring indices possess very similar ppm values.

Our proposed nonlinear intensity shrinkage method overcomes the limitations of existing linear models by leveraging phase-free magnitude and power spectra from the full NMR data, including both absorption and dispersion data, the later are typically discarded in traditional approaches. This enables the derivation of absorption spectra without the need for specific phase error correction models

or optimization function choices, streamlining and enhancing accurate phase error correction in NMR spectroscopy.

While theoretically phase-error-free, real-world spectra may still contain other distortions, such as random errors, similar to those affecting all other variables.

## 2.2. Multiple linear phase models

In addition to the nonlinear intensity shrinkage method, we propose multiple linear phase correction models. While the nonlinear intensity shrinkage method is a novel approach that effectively addresses information loss and can handle nonlinear phase errors, the multiple linear phase models extend the capabilities of existing linear models specifically for addressing nonlinear phase errors.

Our solution involves multiple models for phase error correction. These models operate on sub-ranges defined by major peak ranges, addressing phase errors within each sub-range to effectively mitigate errors across all signals. Refer to Supplement 2 for more details.

## 2.3. Optimization function: delta absolute net minimization (DANM)

Traditional modeling techniques are ineffective for correcting phase errors because no single existing optimization function can adequately optimize model parameters to correct all phase errors. *Current functions do not consider that an ideal signal peak should simultaneously have a maximum positive area and a minimum negative area, leading to suboptimal parameters and phased spectra.* To improve performance, we propose a novel optimization function that minimizes the difference between the absolute and net areas under a curve:

$$(\hat{a}, \hat{b}) = \underset{(a,b)}{\operatorname{argmin}}(\sum_{k=1}^N |A'_k| - \sum_{k=1}^N A'_k) \quad (7)$$

Here,  $(\hat{a}, \hat{b})$  represents the optimal pair for the linear model parameters  $(a, b)$ , while  $\underset{(a,b)}{\operatorname{argmin}}$  denotes the action of

finding the pair  $(a, b)$  that minimizes the function, thereby obtaining the optimal values for  $(a, b)$ .  $A'_k$  is the observed absorption value at the  $k$ -th data point, and  $k$  ranges from 1 to  $N$ , where  $N$  is the total length of the spectrum.

Our new optimization function improves phase error correction by simultaneously minimizing the absolute area while maximizing the net area. This dual-objective strategy effectively addresses the limitations of existing functions, which struggle to balance positive and negative areas, ultimately providing a more accurate and reliable correction of phase errors.

## 3. Materials and Methods

Seven phase error correction methods are compared using simulated data sets, a case study, and metabolite spike-in experiments.

### 3.1. Phase error correction methods

As discussed earlier, many existing optimization functions have limitations when applied to phase error correction. To address these challenges, we focus on three primary functions used in traditional single linear phase correction models: the integral of the imaginary component, the integral of the absolute real part, and entropy. These functions, along with the most commonly used linear phase error correction model, serve as the foundation for comparing the new methods we introduce.

We evaluated seven phase error correction methods, which include three existing methods (SPC\_AAM, SPC\_EMP, and SPC\_DSM) and four new ones (SPC\_DANM, MPC\_DANM, MPC\_EMP, and NLS). The seven methods are as follows:

- SPC\_AAM: A single phase correction model (SPC) with absolute area minimization (AAM) [32, 33].
- SPC\_EMP: A single phase correction model (SPC) with entropy minimization and a negative peak penalty (EMP). Entropy is calculated as the negative sum of absolute intensity multiplied by the logarithm of absolute intensity. A single phase correction model (SPC) [52], with the negative peak penalty defined by the sum of squared negative values [32].
- SPC\_DSM: A single phase correction model (SPC) with dispersion summation minimization (DSM) [52].
- SPC\_DANM: A single phase correction model (SPC) with delta absolute net area minimization (DANM).
- MPC\_DANM: Multiple linear phase correction models (MPC) combined with delta absolute net area minimization (DANM).
- MPC\_EMP: Multiple linear phase correction models (MPC) entropy minimization and a negative peak penalty (EMP).
- NLS: A nonlinear intensity shrinkage method.

All methods, except NLS, rely on specific optimization functions to determine the optimal parameters for phase error correction. Detailed descriptions of the optimization functions and formulas for each method are provided in Supplement 3. Despite differences in the optimization functions or the use of single versus multiple models, the overall optimization process remains consistent across all methods, as outlined in Supplement 4.

## 3.2. Simulations

### 3.2.1. Simulation methods

To generate simulated data for comparing phase error correction methods, we began by creating an idealized spectrum of 76 peaks based on online metabolite features. We then designed three sets of simulated datasets based on this idealized spectrum:

- Nset (noise set): 1,000 datasets with added noise.
- NPset (noise and phase error set): 1,000 datasets with added noise and phase errors.
- NPBset (noise, phase error, and baseline bias set): 1,000 datasets with added noise, phase errors, and baseline bias.

For a more detailed description of these simulations, please refer to Supplement 5.

### 3.2.2. Method comparisons with simulated datasets

We compared seven different methods and the naïve method, with no phase error correction (NPC). Graphical comparisons are detailed in Supplement 6. Using the two most commonly employed error metrics—L1 error (sum of absolute deviations) and L2 error (sum of squared errors)—we assessed each method's performance against the true data. Furthermore, since all methods had the same sample size, we used the ratio of their L2 errors directly for F-tests to compare their variances, as detailed in Supplement 7.

We then used a mixed-effect model to account for internal spatial correlations among peaks and peak ranges within a given spectrum, as well as correlations among spectra within a given simulation dataset. The model was designed to compare methods for phasing the spectra after adjusting for other variables as follows:

$$\Delta Y \sim X_1 + X_3 + (1|X_2/X_4) + E \quad (8)$$

Here,  $\Delta Y = Y - Y_I$  represents the estimation error, where  $Y$  is the estimated peak height or peak range area  $Y$ , and  $Y_I$  is the corresponding value based on the idealized spectrum.  $X_1$  is a factor representing a phase correction method,  $X_2$  denotes a type of simulated dataset (Nset, NPset, or NPBset),  $X_3$  identifies the peak or peak range location, and  $X_4$  identifies the simulated spectra. The random effect structure  $(1|X_2/X_4)$  accounts for variability due to different simulation datasets ( $X_2$ ) and nested effects of spectra ( $X_4$ ) within each dataset ( $X_2$ ), while  $E$  captures random error in the model. To implement this model in R (<https://www.r-project.org/>) based on the lme4 package, use the following example code:

```
library(lme4)
model <- lmer(DeltaY ~ X1 + X3
              + (1|X2/X4), data = dat)
```

To obtain 95% confidence intervals, we used the sim function in the R package arm (<https://cran.r-project.org/web/packages/arm/index.html>) to generate

10,000 simulations. Standard deviations for these simulations were then calculated based on their coefficients.

## 3.3. A case study

The goal of this case study was to evaluate phase error correction methods for detecting glucose concentration differences between healthy individuals and those with early-stage type 2 diabetes mellitus (T2DM) using NMR data. NMR spectra from 25 healthy volunteers and 25 T2DM patients were obtained using the ASICSdata R package [68], sourced from the MetaboLights database (<https://www.ebi.ac.uk/metabolights/>, study MTBLS1), and pre-processed with ACD/1D NMR Manager 8.0 [69].

Our focus was specifically on comparing glucose levels using NMR spectra, despite the availability of more direct measurement methods in hospital laboratories or portable devices. This approach enabled us to evaluate how effectively the phase error correction methods detect subtle variations in glucose levels at early stages. We evaluated seven phase error correction methods alongside the original ASICSdata phased with ACD/1D NMR Manager 8.0, focusing on two glucose multiplets defined by their ranges: 4.63-4.67 ppm and 5.22-5.26 ppm, as identified in ASICSdata (Supplement 8). To improve area estimation stability, we combined the areas of these multiplets.

Methods were clustered based on glucose peak area correlation coefficients, and linear regression models were employed to detect differences in glucose area between diabetics and non-diabetics.

## 3.4. Metabolite spike-in experiments

Simulation studies simplify phase error correction method comparisons but may not accurately represent real NMR data. Direct comparison of methods using real NMR data is challenging due to the absence of a phase error-free spectrum. To address the limitations of both simulation studies and real NMR case studies, we performed spike-in experiments with eight metabolites in three commercial urine samples. Single and Multiple spike-in experiments evaluated phase error correction methods by comparing concentration estimates with known values.

In the single spike-in experiment, creatinine was spiked in at 12 different concentration levels (0-15 mM) to obtain peak area to concentration transformation coefficients. The other seven metabolites were spiked in at six different concentration levels (0-3 mM), and a non-spike-in spectrum was included as a reference (Supplement 9).

In the multiple spike-in experiment, we selected three non-zero concentration levels, including low, medium, and high levels for each metabolite. For creatinine, the actual concentrations for the three levels were 0.5, 5, and 10 mM, while for the other seven metabolites, the concentrations were 0.25, 1, and 3 mM. A concentration level (low,

medium, or high) was randomly selected for each of the eight metabolites, resulting in six distinct concentration combinations. The concentrations were manually adjusted to ensure balance, leading to six final concentration combinations for the eight metabolites (Supplement 9).

Details on sample preparation for  $^1\text{H}$  NMR analysis, spectroscopy data acquisition, and preprocessing can be found in Supplement 9. One of us (AG) defined the range for each metabolite, which could include a single peak or a multiplet. The areas under the curves for these metabolites were then calculated within these defined ranges. To prevent negative concentration estimates, we computed the signal areas for the metabolite spike-in experiments using absolute values. This approach ensured that concentration values remained positive, making the results more meaningful and interpretable.

We used both creatinine peak ranges in the single metabolite spike-in experiment to estimate the area and calculate the coefficient for determining concentration. For the multiple spike-in experiment, we applied the same area-to-concentration transformation coefficient obtained from the single metabolite experiment with creatinine. To ensure consistency, we used only one creatinine peak in the multiple spike-in experiment, similar to other metabolites. Specifically, we selected the peak with three protons at 3 ppm for estimating both the area and concentration.

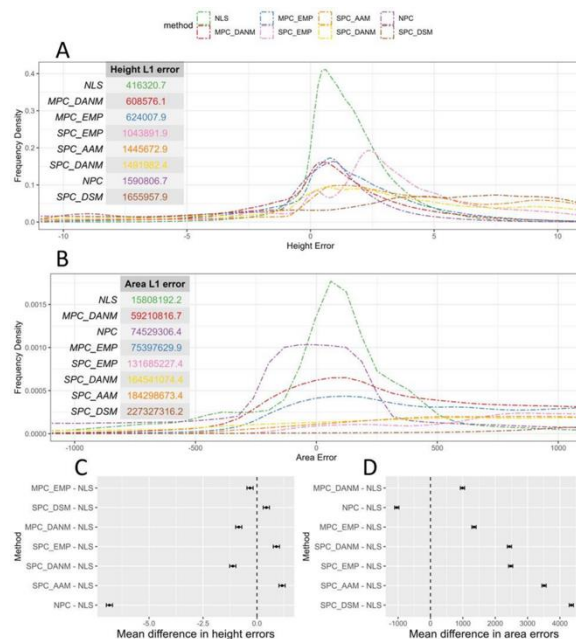
We compared the seven phase error correction methods using concentration estimation error distribution patterns, correlation heatmaps, L1 and L2 errors, F-test statistics, fixed and mixed models. In the single metabolite spike-in experiment, we ignored spectrum information and used a fixed effect model because each spectrum contained only one metabolite, leaving us no choice. In the multiple metabolite spike-in experiment, we used a mixed effect model to address correlations among multiple metabolites within the same spectrum, which is preferable to a fixed effect model that treats each metabolite independently. When combining the results, we had to use a fixed effect model due to the single metabolite experiment's design. Although this is not ideal for the multiple metabolite experiment, it is still reasonable and allows for an integrated analysis that adjusts for differences between the experiments. For additional details on the experimental design and data analysis methods used in the metabolite spike-in experiments, please refer to Supplement 9.

## 4. Results

### 4.1. Comparison of phase error correction methods in simulations

We compared different phase error correction methods using graphic comparisons on simulation data sets. We compared peak height error (Supplement 10), peak range error (Supplement 11), and point-to-point intensity error (Supplement 12), and all metrics showed that the nonlinear intensity shrinkage (NLS) method performed the best.

**Figure 5**  
Comparisons of phase error correction methods in simulation data sets



L1 errors and empirical density plots of peak height error (A) and peak range area error (B), highlighting details around zero. Comparison of different methods against NLS within a peak error mixed model (C) and within a peak range area error mixed model (D). Abbreviations: MPC\_DANM: multiple models with delta absolute net minimization, MPC\_EMP: multiple models minimizing entropy with negative peak penalty, NLS: nonlinear shrinkage, NPC: no phase error correction, SPC\_AAM: a single model minimizing the absolute area, SPC\_DANM: a single model with delta absolute net minimization, SPC\_DSM: single model minimizing dispersion sum, and SPC\_EMP: a single model minimizing entropy with negative peak penalty. We then aggregated and compared the peak height errors and the peak range area errors (Supplement 13, Figures 5A-B), which showed that the NLS has the smallest L1 error and the highest error peak around 0, indicating the highest accuracy and precision.

We also conducted peak height error and peak range area error comparison by L1 error and L2 error across three simulation datasets, and F test on L2 error with NLS as the reference level. Comparisons showed that the NLS method had the smallest errors for both L1 and L2 errors, while the two multiple model methods were the second-best. Furthermore, the NLS method was significantly better than all other methods based on the F test (Supplement 14).

We then fitted peak height error and peak range area error mixed models to compare different phase error correction methods after adjusting for peak or peak range effect, the random effect of the simulation datasets, and the random effect of the spectra within each simulation dataset. The full mixed model results are shown in Supplement 15. The method comparison parts for peak height error and peak



Next, we examine the correlation of the performance of these seven methods. The correlation heatmap of the seven phase error correction methods, based on metabolite concentration errors, revealed that the four best-performing methods, MPC\_EMP, MPC\_DANM, SPC\_DANM, and NLS, were highly correlated with each other compared to other single model-based methods (Supplement 17).

We then compared the L2 errors of the seven phase error correction methods. In the single metabolite spike-in experiment, the multiple model approach optimized with delta absolute net minimization (MPC\_DANM) had the smallest L2 errors (Table 1). F-tests showed significant differences between MPC\_DANM and all other methods except for MPC\_EMP, which is also based on multiple models (Table 1).

**Table 1**  
**L1, L2, and F-test values for the single metabolite spike-in experiment. MPC\_DANM, the method with the smallest L2 error, is used as the reference in the F-test (degrees of freedom = 170)**

Method	L1 error	L2 error	F	P value (one tail)
SPC_AAM	187.9	730.6	9.65	< 0.0001***
SPC_EMP	149.96	435.06	5.75	< 0.0001***
SPC_DSM	445.16	3700.99	48.91	< 0.0001***
SPC_DANM	107.47	308.52	4.08	< 0.0001***
MPC_DANM	75.45	75.68	1	0.5
MPC_EMP	78.37	83.38	1.1	0.2639
NLS	97.7	108.91	1.44	0.0091**

**Table 2**  
**L1, L2, and F-test values for the multiple metabolite spike-in experiment. SPC\_DANM, the method with the smallest L2 error, is used as the reference in the F-test (degrees of freedom = 197)**

Method	L1 error	L2 error	F	P value (one tail)
SPC_AAM	290.44	978.84	2.12	< 0.0001***
SPC_EMP	326.43	1274.57	2.76	< 0.0001***
SPC_DSM	1357.75	28002.27	60.55	< 0.0001***
SPC_DANM	165.16	462.49	1	0.5
MPC_DANM	210.95	769.38	1.66	0.0002***
MPC_EMP	217.15	879.89	1.9	< 0.0001***
NLS	185.24	563.83	1.22	0.0826

**Table 3**  
**L1, L2, and F-test values for combination of both the single and multiple spike-in experiments. NLS, the method with the smallest L2 error, is used as the reference in the F-test (degrees of freedom = 368)**

Method	L1 error	L2 error	F	P value (one tail)
SPC_AAM	478.35	1709.44	2.54	< 0.0001***
SPC_EMP	476.38	1709.63	2.54	< 0.0001***
SPC_DSM	1802.91	31703.3	47.13	< 0.0001***
SPC_DANM	272.63	771.01	1.15	0.0957
MPC_DANM	286.4	845.06	1.26	0.0145*
MPC_EMP	295.51	963.28	1.43	0.0003**
NLS	282.94	672.74	1	0.5

In the multiple metabolite spike-in experiment, a single model with delta absolute net minimization (SPC\_DANM) had the smallest L2 errors (Table 2). F-tests showed significant differences between this method and all other methods except the nonlinear shrinkage (NLS) (Table 2).

When we combined the results of these two experiments, Table 3 showed that NLS had the smallest L2 error. F-tests showed that all other methods were significantly different from NLS except SPC\_DANM.

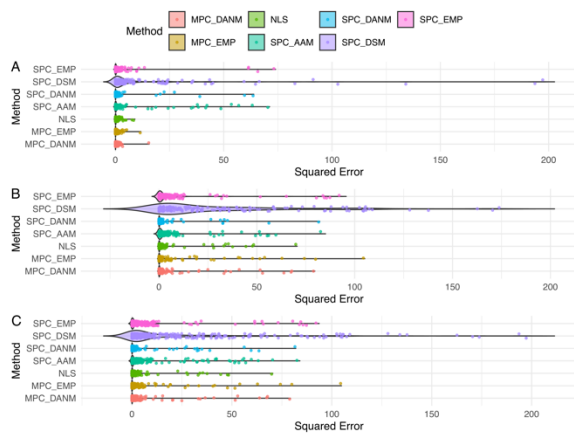
Full model analyses were conducted not only on phase correction methods but also on metabolites and urine samples, as detailed in Supplement 18. This supplement includes all modeling results for the single metabolite spike-in experiment, the multiple metabolite spike-in experiment, and the combination of these two experiments. Forest plots in Figures 7D-E display the comparison of methods after adjusting for urine sample and metabolite effects in the complete models. The method with the smallest L2 error was used as the reference level for each model. In the single metabolite experiment, none of the methods showed significant differences from the multiple model approach with delta absolute net minimization (MPC\_DANM). In the multiple metabolite experiment, only the single model optimized with dispersion (SPC\_DSM) showed a significant difference when compared to the single model optimized with delta absolute net minimization (SPC\_DANM). When both experiments were combined, all methods did not have significant differences from the nonlinear shrinkage (NLS) method, except for SPC\_DSM.

Although Figure 7 shows the distribution of errors from the experiments and provides a good visualization of errors, it treats all error units equally. In contrast, squared errors can penalize errors that are further from zero. This distinction is why the sum of squared errors (L2 errors) is widely used in statistics and serves as the basis for the main comparisons in Tables 1-3.

To help visualize the squared errors, Figure 8 presents their

distribution for the metabolite spike-in experiments. It is clear that NLS consistently has the smallest ranges of squared errors, whether in the single spike-in experiment (Figure 8A), the multiple spike-in experiment (Figure 8B), or a combination of both experiments (Figure 8C). Even the L2 error of NLS is not always the smallest, as shown in Tables 1-3.

**Figure 8**  
**Distribution of squared errors for metabolite spike-in experiments**



Violin plots with jittered data points of squared errors in metabolite concentration estimation for the single spike-in experiment (A), the multiple metabolite spike-in experiment (B), and the combination of both (C). To save space, extreme outliers from SPC\_DSM have been omitted.

Based on our statistical analysis of metabolite spike-in experiments, we consistently observed that SPC\_DSM performed worse compared to the other methods across multiple scenarios. This consistent underperformance supports our conclusion that SPC\_DSM is the least effective method among the seven we tested. On the other hand, our new optimization function with a single model (SPC\_DANM) or multiple models (MPC\_DANM), as well as nonlinear shrinkage (NLS) are good performers.

## 5. Discussion

Phase error correction is a critical pre-processing step in NMR. Existing methods typically use a single-phase error correction model for the entire spectrum and heavily depend on the optimization function. In this paper, we introduced two new approaches, nonlinear shrinkage (NLS) with full information and MPC with multiple phase error correction models, along with a new optimization function called delta absolute net minimization (DANM). NLS and DANM represent our key innovations, while MPC modifies existing models by dividing the spectrum into peak ranges and applies a phase correction model to each range.

Simulations and the case study demonstrated that NLS was the top performer, significantly faster than other methods, as

it does not require any optimization process. In the metabolite spike-in experiments, MPC\_DANM and SPC\_DANM were the top performers based on L2 errors in the single spike-in and multiple spike-in experiments, respectively. However, when the results of both experiments were combined, NLS emerged as the best method based on L2 errors. Furthermore, when examining the distribution of squared errors, NLS consistently exhibited the narrowest error ranges across the single spike-in, multiple spike-in, and combined experiments.

Although the results from the metabolite experiments were more complex compared to the simulations, we conclude that NLS remains the most reliable method for phase error correction and is also the fastest. Its advantage lies in avoiding the inherent approximations of optimization, relying instead on the solid theoretical support we demonstrated mathematically in Section 2.

Our new optimization function, DANM, also showed strong results in enhancing phase error correction, whether applied to single or multiple models. This highlights the versatility of DANM, whose performance remained consistent regardless of the number of models used. Both NLS and DANM offer promising potential to be extended beyond the 1D data used here to 2D and 3D NMR applications.

In contrast, our modified MPC approach did not show the significant performance gains we initially expected, and its success is highly dependent on the optimization function used. Therefore, we do not recommend MPC for general use.

SPC\_DSM, on the other hand, performed the worst across all simulations, the case study, and metabolite spike-in experiments. As discussed in our phase error correction review [51], minimizing the integral of the dispersion component can be misleading. Ideally, when no phase error is present, the integral of the dispersion component should be zero, but not necessarily minimal. To address this, we suggested minimizing the absolute integral instead [51]; however, this introduced a new problem—non-differentiability at zero—resulting in poor convergence. When we tested this revised version alongside the single-model approach, SPC\_DSM remained the worst performer (data not shown). This shows the difficulty in effectively incorporating the dispersion component into the optimization process.

The other two optimization functions, AAM and EMP, performed better than DSM, though not as effectively as DANM, with their performance being quite close. Thus, relying on DANM alone cannot significantly improve phase error correction performance. Looking at the broader picture, we have tested many different optimization functions, yet none have completely resolved the phase error problem.

While NLS does not rely on any optimization function, it also does not consistently outperform other methods, as demonstrated in our metabolite spike-in experiments. To further improve its performance, we need to address potential issues related to sub-range divisions. Although NLS should theoretically yield an ideal real part, it depends

on dividing the spectrum into peak ranges, which can lead to non-smooth transitions between neighboring ranges. Additionally, within the same peak range, smaller peaks may shrink excessively. Overall, dividing a spectrum is challenging due to noise, cutoffs, and overlapping signals.

All the methods discussed in this paper, including additional options, are available in the R package NMRphasing, accessible via GitHub (<https://github.com/ajiangsfu/NMRphasing>) and CRAN (<https://cran.r-project.org/web/packages/NMRphasing/index.html>).

Looking forward, although we did not apply neural networks in this research, our phase error correction review [51] highlights the challenges of using neural networks, especially the reliance on optimization functions based on squared or absolute errors, which require ground truth that is not available in real-world MR data. This limitation explains why phase errors can still persist even after adjustments with neural networks.

Despite the limitations of each individual approach, combining them could lead to significant improvements in phase error correction. For instance, instead of using L1 or L2 errors for neural network training, we could apply MR-specific optimization functions like DANM, thereby eliminating the need for ground truth. Alternatively, we could use NLS-phased MR data as pseudo ground truth. Although NLS is not perfect, it offers the closest approximation for well-separated peaks in real-world MR data. The future direction lies in integrating the strengths of multiple approaches while mitigating their individual weaknesses.

## Ethical Statement

This study does not contain any studies with human or animal subjects performed by any of the authors.

## Conflicts of Interest

The authors declare that they have no conflicts of interest to this work.

## Data Availability Statement

Data available on request from the corresponding author upon reasonable request.

## Author Contribution Statement

**Aixiang Jiang:** Conceptualization, Methodology, Software, Validation, Formal analysis, Investigation, Data curation, Writing - original draft, Writing - review & editing, Visualization, Supervision, Project administration. **Andr e**

**E. Gravel:** Resources, Data curation, Writing - review & editing. **Ethan Tse:** Writing - review & editing. **Sanjoy Kumar Das:** Resources, Data curation. **James Hanley:** Conceptualization, Writing - original draft, Writing - review & editing, Supervision, Project administration. **Robert Nadon:** Conceptualization, Resources, Data curation, Writing - original draft, Writing - review & editing, Supervision, Project administration.

## References

- [1] Akoka, S., & Remaud, G. S. (2020). NMR-based isotopic and isotopomic analysis. *Progress in Nuclear Magnetic Resonance Spectroscopy*, 120–121, 1–24. <https://doi.org/10.1016/j.pnmrs.2020.07.001>
- [2] Anaraki, M. T., Lysak, D. H., Downey, K., Kock, F. V. C., You, X., Majumdar, R. D., ..., & Simpson, A. J. (2021). NMR spectroscopy of wastewater: A review, case study, and future potential. *Progress in Nuclear Magnetic Resonance Spectroscopy*, 126, 121–180. <https://doi.org/10.1016/j.pnmrs.2021.08.001>
- [3] Chandler, B., Todd, L., & Smith, S. O. (2022). Magic angle spinning NMR of G protein-coupled receptors. *Progress in Nuclear Magnetic Resonance Spectroscopy*, 128, 25–43. <https://doi.org/10.1016/j.pnmrs.2021.10.002>
- [4] Dalvit, C., Gm ur, I., R obler, P., & Gossert, A. D. (2023). Affinity measurement of strong ligands with NMR spectroscopy: Limitations and ways to overcome them. *Progress in Nuclear Magnetic Resonance Spectroscopy*, 138–139, 52–69. <https://doi.org/10.1016/j.pnmrs.2023.07.001>
- [5] Damodaran, K. (2022). Recent advances in NMR spectroscopy of ionic liquids. *Progress in Nuclear*

- Magnetic Resonance Spectroscopy*, 129, 1–27.  
<https://doi.org/10.1016/j.pnmrs.2021.12.001>
- [6] Eills, J., Hale, W., & Utz, M. (2022). Synergies between Hyperpolarized NMR and Microfluidics: A Review. *Progress in Nuclear Magnetic Resonance Spectroscopy*, 128, 44–69.  
<https://doi.org/10.1016/j.pnmrs.2021.09.001>
- [7] Forse, A. C., Merlet, C., Grey, C. P., & Griffin, J. M. (2021). NMR studies of adsorption and diffusion in porous carbonaceous materials. *Progress in Nuclear Magnetic Resonance Spectroscopy*, 124–125, 57–84.  
<https://doi.org/10.1016/j.pnmrs.2021.03.003>
- [8] Jones, J. A. (2024). Controlling NMR spin systems for quantum computation. *Progress in Nuclear Magnetic Resonance Spectroscopy*, 140–141, 49–85. <https://doi.org/10.1016/j.pnmrs.2024.02.002>
- [9] Krivdin, L. B. (2023). An overview of Helium-3 NMR: Recent developments and applications. *Progress in Nuclear Magnetic Resonance Spectroscopy*, 136–137, 83–109.  
<https://doi.org/10.1016/j.pnmrs.2023.08.001>
- [10] Kupče, Ě., Mote, K. R., Webb, A., Madhu, P. K., & Claridge, T. D. W. (2021). Multiplexing experiments in NMR and multi-nuclear MRI. *Progress in Nuclear Magnetic Resonance Spectroscopy*, 124–125, 1–56.  
<https://doi.org/10.1016/j.pnmrs.2021.03.001>
- [11] Leifer, N., Aurbach, D., & Greenbaum, S. G. (2024). NMR studies of lithium and sodium battery electrolytes. *Progress in Nuclear Magnetic Resonance Spectroscopy*, 142–143, 1–54.  
<https://doi.org/10.1016/j.pnmrs.2024.02.001>
- [12] Middleton, D. A. (2024). NMR studies of amyloid interactions. *Progress in Nuclear Magnetic Resonance Spectroscopy*, 144–145, 63–96.  
<https://doi.org/10.1016/j.pnmrs.2024.07.001>
- [13] Mishra, S. K., & Suryaprakash, N. (2023). Pure shift edited NMR methodologies for the extraction of Homo- and heteronuclear couplings with ultra-high resolution. *Progress in Nuclear Magnetic Resonance Spectroscopy*, 136–137, 1–60.  
<https://doi.org/10.1016/j.pnmrs.2023.02.001>
- [14] Neuhaus, D. (2022). Zinc finger structure determination by NMR: Why zinc fingers can be a handful. *Progress in Nuclear Magnetic Resonance Spectroscopy*, 130–131, 62–105.  
<https://doi.org/10.1016/j.pnmrs.2022.07.001>
- [15] Pavón, E., & Alba, M. D. (2021). Swelling layered minerals applications: A solid state NMR overview. *Progress in Nuclear Magnetic Resonance Spectroscopy*, 124–125, 99–128.  
<https://doi.org/10.1016/j.pnmrs.2021.04.001>
- [16] Snyder, D. A. (2021). Covariance NMR: Theoretical concerns, practical considerations, contemporary applications and related techniques. *Progress in Nuclear Magnetic Resonance Spectroscopy*, 122, 1–10.  
<https://doi.org/10.1016/j.pnmrs.2020.09.001>
- [17] Theillet, F.-X., & Luchinat, E. (2022). In-cell NMR: Why and how? *Progress in Nuclear Magnetic Resonance Spectroscopy*, 132–133, 1–112.

- <https://doi.org/10.1016/j.pnmrs.2022.04.002>
- [18] Tugarinov, V., Cecon, A., & Clore, G. M. (2022). NMR methods for exploring ‘dark’ states in ligand binding and protein-protein interactions. *Progress in Nuclear Magnetic Resonance Spectroscopy*, 128, 1–24. <https://doi.org/10.1016/j.pnmrs.2021.10.001>
- [19] Tugarinov, V., & Clore, G. M. (2024). The utility of small nutation angle 1H pulses for NMR studies of methyl-containing side-chain dynamics in proteins. *Progress in Nuclear Magnetic Resonance Spectroscopy*, 144–145, 40–62. <https://doi.org/10.1016/j.pnmrs.2024.05.004>
- [20] Vosegaard, T. (2021). Single-crystal NMR spectroscopy. *Progress in Nuclear Magnetic Resonance Spectroscopy*, 123, 51–72. <https://doi.org/10.1016/j.pnmrs.2021.01.001>
- [21] Xu, G., Cheng, K., Liu, M., & Li, C. (2024). Studying protein stability in crowded environments by NMR. *Progress in Nuclear Magnetic Resonance Spectroscopy*, 140–141, 42–48. <https://doi.org/10.1016/j.pnmrs.2024.01.001>
- [22] Zheng, M., Chu, Y., Wang, Q., Wang, Y., Xu, J., & Deng, F. (2024). Advanced solid-state NMR spectroscopy and its applications in zeolite chemistry. *Progress in Nuclear Magnetic Resonance Spectroscopy*, 140–141, 1–41. <https://doi.org/10.1016/j.pnmrs.2023.11.001>
- [23] Ernst, R. R., Bodenhausen, G., & Wokaun, A. (1987). *Principles of Nuclear Magnetic Resonance in One and Two Dimensions*. UK: Clarendon Press.
- [24] Keeler, J. (2011). *Understanding NMR Spectroscopy*. USA: Wiley. [https://books.google.co.uk/books?id=PKQlfaK4COoC&lpg=PR17&ots=ydJiBq4Z6M&dq=Keeler%2C%20J.%20\(2011\).%20Understanding%20MR%20Spectroscopy.%20Wiley.&lr&hl=zh-CN&pg=PR17#v=onepage&q&f=false](https://books.google.co.uk/books?id=PKQlfaK4COoC&lpg=PR17&ots=ydJiBq4Z6M&dq=Keeler%2C%20J.%20(2011).%20Understanding%20MR%20Spectroscopy.%20Wiley.&lr&hl=zh-CN&pg=PR17#v=onepage&q&f=false)
- [25] He, T., Zur, Y., Montrazi, E. T., & Frydman, L. (2024). Phase-incremented steady-state free precession as an alternate route to high-resolution NMR. *Journal of the American Chemical Society*, 146(6), 3615–3621. <https://doi.org/10.1021/jacs.3c12954>
- [26] Jiang, A. (2024a). Insights into nuclear magnetic resonance data pre-processing: A Comprehensive review. *Journal of Data Science and Intelligent Systems*. <https://doi.org/10.47852/bonviewJDSIS42022556>
- [27] Minderhoud, S. C. S., van der Velde, N., Wentzel, J. J., van der Geest, R. J., Attrach, M., Wielopolski, P. A., Budde, R. P. J., ..., & Hirsch, A. (2020). The clinical impact of phase offset errors and different correction methods in cardiovascular magnetic resonance phase contrast imaging: A multi-scanner study. *Journal of Cardiovascular Magnetic Resonance: Official Journal of the Society for Cardiovascular Magnetic Resonance*, 22(1), 68. <https://doi.org/10.1186/s12968-020-00659-3>
- [28] Abdulla, S. U., Reutens, D., Bollmann, S., & Vegh, V. (2020). MRI phase offset correction method impacts quantitative susceptibility mapping.

- Magnetic Resonance Imaging*, 74, 139–151.  
<https://doi.org/10.1016/j.mri.2020.08.009>
- [29] Wymer, D. T., Patel, K. P., Burke, W. F., & Bhatia, V. K. (2020). Phase-contrast MRI: Physics, techniques, and clinical applications. *RadioGraphics*, 40(1), 122–140.  
<https://doi.org/10.1148/rg.2020190039>
- [30] Bao, Q., Feng, J., Chen, L., Chen, F., Liu, Z., Jiang, B., & Liu, C. (2013). A robust automatic phase correction method for signal dense spectra. *Journal of Magnetic Resonance*, 234, 82–89.  
<https://doi.org/10.1016/j.jmr.2013.06.012>
- [31] Chen, L., Weng, Z., Goh, L., & Garland, M. (2002). An efficient algorithm for automatic phase correction of NMR spectra based on entropy minimization. *Journal of Magnetic Resonance*, 158(1), 164–168.  
[https://doi.org/10.1016/S1090-7807\(02\)00069-1](https://doi.org/10.1016/S1090-7807(02)00069-1)
- [32] de Brouwer, H. (2009). Evaluation of algorithms for automated phase correction of NMR spectra. *Journal of Magnetic Resonance*, 201(2), 230–238.  
<https://doi.org/10.1016/j.jmr.2009.09.017>
- [33] Džakula, Ž. (2000). Phase angle measurement from peak areas (PAMPAS). *Journal of Magnetic Resonance*, 146(1), 20–32.  
<https://doi.org/10.1006/jmre.2000.2123>
- [34] Mikkelsen, M., Tapper, S., Near, J., Mostofsky, S. H., Puts, N. A. J., & Edden, R. A. E. (2020). Correcting frequency and phase offsets in MRS data using robust spectral registration. *NMR in Biomedicine*, 33(10), e4368.  
<https://doi.org/10.1002/nbm.4368>
- [35] Prostko, P., Pikkemaat, J., Selter, P., Lukasczek, M., Wechselberger, R., Khamiakova, T., & Valkenburg, D. (2022). R shiny app for the automated deconvolution of NMR spectra to quantify the solid-state forms of pharmaceutical mixtures. *Metabolites*, 12(12).  
<https://doi.org/10.3390/metabo12121248>
- [36] Rout, M., Lipfert, M., Lee, B. L., Berjanskii, M., Assempour, N., Fresno, R. V., ..., & Wishart, D. S. (2023). MagMet: A fully automated web server for targeted nuclear magnetic resonance metabolomics of plasma and serum. *Magnetic Resonance in Chemistry*, 61(12), 681–704.  
<https://doi.org/10.1002/mrc.5371>
- [37] Sakhaei, P., Bohorc, B., Schliedermann, U., & Bermel, W. (2021). Boosting the resolution of multidimensional NMR spectra by complete removal of proton spin multiplicities. *Scientific Reports*, 11(1), 21566.  
<https://doi.org/10.1038/s41598-021-01041-8>
- [38] Van, A. T., Hernando, D., & Sutton, B. P. (2011). Motion-induced phase error estimation and correction in 3D diffusion tensor imaging. *IEEE Trans Med Imaging*, 30(11), 1933–1940.  
<https://doi.org/10.1109/TMI.2011.2158654>
- [39] Worley, B., & Powers, R. (2014). Simultaneous phase and scatter correction for NMR datasets. *Chemometr Intell Lab Syst*, 131, 1–6.  
<https://doi.org/10.1016/j.chemolab.2013.11.005>
- [40] Wright, A. J., Buydens, L. M., & Heerschap, A. (2012). A phase and frequency alignment protocol for  $^1\text{H}$

- MRSI data of the prostate. *NMR Biomed*, 25(5), 755–765. <https://doi.org/10.1002/nbm.1790>
- [41] Yong, J. (2024). NMR Theory. In J. Yong (Ed.), *Optimising NMR Spectroscopy Through Method and Software Development* (pp. 1–33). Springer Nature Switzerland. [https://doi.org/10.1007/978-3-031-46684-7\\_1](https://doi.org/10.1007/978-3-031-46684-7_1)
- [42] Gan, Z., & Hung, I. (2022). Second-order phase correction of NMR spectra acquired using linear frequency-sweeps. *Magnetic Resonance Letters*, 2(1), 1–8. <https://doi.org/10.1016/j.mrl.2021.100026>
- [43] Jaroszewicz, M. J., Altenhof, A. R., Schurko, R. W., & Frydman, L. (2023). An automated multi-order phase correction routine for processing ultra-wideline NMR spectra. *Journal of Magnetic Resonance*, 354, 107528. <https://doi.org/10.1016/j.jmr.2023.107528>
- [44] Mattay, R. R., Kim, K., Shah, L., Shah, B., Sugrue, L., Safoora, F., ..., & Narsinh, K. H. (2023). MR thermometry during transcranial MR imaging-guided focused ultrasound procedures: A review. *American Journal of Neuroradiology*. <https://doi.org/10.3174/ajnr.A8038>
- [45] Srinivas, S., Masutani, E., Norbash, A., & Hsiao, A. (2023). Deep learning phase error correction for cerebrovascular 4D flow MRI. *Scientific Reports*, 13(1), 9095. <https://doi.org/10.1038/s41598-023-36061-z>
- [46] van Vaals, J. J., & van Gerwen, P. H. J. (1990). Novel methods for automatic phase correction of NMR spectra. *Journal of Magnetic Resonance* (1969), 86(1), 127–147. [https://doi.org/10.1016/0022-2364\(90\)90216-V](https://doi.org/10.1016/0022-2364(90)90216-V)
- [47] You, S., Masutani, E. M., Alley, M. T., Vasanaawala, S. S., Taub, P. R., Liau, J., ..., & Hsiao, A. (2022). Deep learning automated background phase error correction for abdominopelvic 4D flow MRI. *Radiology*, 302(3), 584–592. <https://doi.org/10.1148/radiol.2021211270>
- [48] Ernst, R. R. (1969). Numerical Hilbert transform and automatic phase correction in magnetic resonance spectroscopy. *Journal of Magnetic Resonance* (1969), 1(1), 7–26. [https://doi.org/10.1016/0022-2364\(69\)90003-1](https://doi.org/10.1016/0022-2364(69)90003-1)
- [49] Larry Bretthorst, G. (2008). Automatic phasing of MR images. Part I: Linearly varying phase. *Journal of Magnetic Resonance*, 191(2), 184–192. <https://doi.org/10.1016/j.jmr.2007.12.010>
- [50] Near, J., Harris, A. D., Juchem, C., Kreis, R., Marjańska, M., Öz, G., ..., & Gasparovic, C. (2021). Preprocessing, analysis and quantification in single-voxel magnetic resonance spectroscopy: Experts' consensus recommendations. *NMR in Biomedicine*, 34(5), e4257. <https://doi.org/10.1002/nbm.4257>
- [51] Jiang, A. (2024b). Phase error correction in magnetic resonance: A review of models, optimization functions, and optimizers in traditional statistics and neural networks. *Preprints*. <https://doi.org/10.20944/preprints202409.2252.v1>
- [52] Binczyk, F., Tarnawski, R., & Polanska, J. (2015).

- Strategies for optimizing the phase correction algorithms in Nuclear Magnetic Resonance spectroscopy. *Biomedical Engineering Online*, 14, 1-14. <https://doi.org/10.1186/1475-925X-14-S2-S5>
- [53] Hardy, E. H., Hoferer, J., Mertens, D., & Kasper, G. (2009). Automated phase correction via maximization of the real signal. *Magnetic Resonance Imaging*, 27(3), 393–400. <https://doi.org/10.1016/j.mri.2008.07.009>
- [54] Nelson, S. J., & Brown, T. R. (1989). The accuracy of quantification from 1d NMR spectra using the PIQABLE algorithm. *Journal of Magnetic Resonance*, 84(1), 95–109. [https://doi.org/10.1016/0022-2364\(89\)90008-5](https://doi.org/10.1016/0022-2364(89)90008-5)
- [55] Simicic, D., Zöllner, H. J., Davies-Jenkins, C. W., Hupfeld, K. E., Edden, R. A. E., & Oeltzschner, G. (2024). Model-based frequency-and-phase correction of (1)H MRS data with 2D linear-combination modeling. *Magnetic Resonance in Medicine*, 92(5), 2222–2236. <https://doi.org/10.1002/mrm.30209>
- [56] Brown, D. E., Campbell, T. W., & Moore, R. N. (1989). Automated phase correction of FT NMR spectra by baseline optimization. *Journal of Magnetic Resonance (1969)*, 85(1), 15–23. [https://doi.org/10.1016/0022-2364\(89\)90315-6](https://doi.org/10.1016/0022-2364(89)90315-6)
- [57] Craig, E. C., & Marshall, A. G. (1988). Automated phase correction of FT NMR spectra by means of phase measurement based on dispersion versus absorption relation (DISPA). *Journal of Magnetic Resonance*, 76(3), 458–475. [https://doi.org/10.1016/0022-2364\(88\)90350-2](https://doi.org/10.1016/0022-2364(88)90350-2)
- [58] Ben-Tal, Y., Boaler, P. J., Dale, H. J. A., Dooley, R. E., Fohn, N. A., Gao, Y., ..., & Lloyd-Jones, G. C. (2022). Mechanistic analysis by NMR spectroscopy: A users guide. *Progress in Nuclear Magnetic Resonance Spectroscopy*, 129, 28–106. <https://doi.org/10.1016/j.pnmrs.2022.01.001>
- [59] Canlet, C., Deborde, C., Cahoreau, E., Da Costa, G., Gautier, R., Jacob, D., ..., & Giraudeau, P. (2023). NMR metabolite quantification of a synthetic urine sample: An inter-laboratory comparison of processing workflows. *Metabolomics*, 19(7), 65. <https://doi.org/10.1007/s11306-023-02028-4>
- [60] Corol, D. I., Harflett, C., Beale, M. H., & Ward, J. L. (2014). An efficient high throughput metabotyping platform for screening of biomass willows. *Metabolites*, 4(4), 946–976. PubMed. <https://doi.org/10.3390/metabo4040946>
- [61] del Campo, G., Zuriarrain, J., Zuriarrain, A., & Berregi, I. (2016). Quantitative determination of carboxylic acids, amino acids, carbohydrates, ethanol and hydroxymethylfurfural in honey by (1)H NMR. *Food Chemistry*, 196, 1031–1039. <https://doi.org/10.1016/j.foodchem.2015.10.036>
- [62] Motegi, H., Tsuboi, Y., Saga, A., Kagami, T., Inoue, M., Toki, H., ..., & Kikuchi, J. (2015). Identification of reliable components in multivariate curve resolution-alternating least squares (MCR-ALS): A data-driven approach across metabolic processes. *Scientific Reports*, 5,

- 15710–15710. <https://doi.org/10.1038/srep15710>
- [63] Bugler, H., Berto, R., Souza, R., & Harris, A. D. (2024). Frequency and phase correction of GABA-edited magnetic resonance spectroscopy using complex-valued convolutional neural networks. *Magnetic Resonance Imaging*, *111*, 186–195. <https://doi.org/10.1016/j.mri.2024.05.008>
- [64] Ma, D. J., Yang, Y., Harguindeguy, N., Tian, Y., Small, S. A., Liu, F., ..., & Guo, J. (2024). Magnetic resonance spectroscopy spectral registration using deep learning. *Journal of Magnetic Resonance Imaging*, *59*(3), 964–975. <https://doi.org/10.1002/jmri.28868>
- [65] Shamaei, A., Starcukova, J., Pavlova, I., & Starcuk Jr., Z. (2023). Model-informed unsupervised deep learning approaches to frequency and phase correction of MRS signals. *Magnetic Resonance in Medicine*, *89*(3), 1221–1236. <https://doi.org/10.1002/mrm.29498>
- [66] Fischer, C., Miska, M., Jung, A., Weber, M.-A., Saure, D., Schmidmaier, G., ..., & Doll, J. (2020). Posttraumatic perfusion analysis of quadriceps, patellar, and achilles tendon regeneration with dynamic contrast-enhanced ultrasound and dynamic contrast-enhanced magnetic resonance imaging. *Journal of Ultrasound in Medicine*, *n/a*(n/a). <https://doi.org/10.1002/jum.15424>
- [67] Marshall, A. G., & Verdun, F. R. (1990). *Fourier transforms in NMR, optical, and mass spectrometry: A user's handbook*. USA: Elsevier.
- [68] Lefort, G., Liaubet, L., Canlet, C., Tardivel, P., Père, M.-C., Quesnel, H., ..., & Servien, R. (2019). ASICS: an R package for a whole analysis workflow of 1D 1H NMR spectra. *Bioinformatics (Oxford, England)*, *35*(21), 4356–4363. <https://doi.org/10.1093/bioinformatics/btz248>
- [69] Salek, R. M., Maguire, M. L., Bentley, E., Rubtsov, D. V., Hough, T., Cheeseman, M., ..., & Griffin, J. L. (2007). A metabolomic comparison of urinary changes in type 2 diabetes in mouse, rat, and human. *Physiological Genomics*, *29*(2), 99–108. <https://doi.org/10.1152/physiolgenomics.00194.2006>

## How to Cite